Engineering 22 (2023) 149–158

Contents lists available at ScienceDirect

Engineering

journal homepage: www.elsevier.com/locate/eng

Research
Medical Engineering–Article

Structural and Functional NIR-II Fluorescence Bioimaging in Urinary System via Clinically Approved Dye Methylene Blue

Dingwei Xue [a], Di Wu [b], Zeyi Lu [a], Jochen Neuhaus [c], Abudureheman Zebibula [a], Zhe Feng [d], Sheng Cheng [a], Jing Zhou [d], Jun Qian [a,d,*], Gonghui Li [a,*]

[a] Department of Urology, Sir Run Run Shaw Hospital, School of Medicine, Zhejiang University, Hangzhou 310016, China
[b] Department of General Surgery, Sir Run Run Shaw Hospital, School of Medicine, Zhejiang University, Hangzhou 310016, China
[c] Department of Urology, University of Leipzig, Leipzig 04103, Germany
[d] State Key Laboratory of Modern Optical Instrumentation, Centre for Optical and Electromagnetic Research, College of Optical Science and Engineering, Zhejiang University, Hangzhou 310058, China

ARTICLE INFO

Article history:
Received 10 February 2021
Revised 15 July 2021
Accepted 15 July 2021
Available online 25 April 2022

Keywords:
NIR-II fluorescence
Methylene blue
Renal function
Urinary system
Real-time imaging

ABSTRACT

Accurate structural and functional imaging is vital for the diagnosis and prognosis of urinary system diseases. Fluorescence bioimaging in the second near-infrared spectral region (NIR-II, 1000–1700 nm) has shown advantages of higher spatial resolution, deeper penetration, and finer signal-to-background ratio (SBR) compared to the conventional fluorescence imaging methods but limited to its clinical inapplicability. Herein, we first report *in vivo* NIR-II fluorescence imaging of the urinary system enabled by a clinically approved and renal excretable dye methylene blue (MB), which cannot only achieve clear invasive/non-invasive urography but also noninvasively detect renal function efficiently. These results demonstrate that MB assisted NIR-II fluorescence imaging holds a great promise for structural and functional imaging of the urinary system both clinically and preclinically.

1. Introduction

Diagnosis and prognosis of urinary system diseases were based on imaging tests such as excretory urography, urination cystography (UCG), and urological computerized tomography. However, those methods have disadvantages such as ray exposure, contrast allergy, and poor effectiveness [1–5]. Besides, the need for sensitive, real-time, and safe imaging methods increased along with the number of minimally-invasive procedures being performed.

Noninvasive analysis of renal function is also essential for accessing urinary system diseases, especially unilateral kidney diseases [6]. As the accurate evaluation of renal function demands real-time imaging of kidneys at high contrast and high temporal resolution, currently single-photon emission computed tomography (SPECT), magnetic resonance imaging (MRI), and positron emission tomography (PET) are the major tools for both clinical diagnosis and preclinical renal function studies [7–9]. Likewise, these methods suffered from high cost, limited access, and potential radiation exposure risk. Therefore, safe, low-cost, and sensitive renal functional imaging techniques are extremely desired for clinical and preclinical kidney functional assessment.

Near-infrared (NIR) fluorescence imaging, a promising biomedical imaging method, has shown superior properties in clinical translation owing to its high sensitivity, high temporal resolution, and fast feedback, but is restricted to limited penetration depth [10–13]. As imaging modality improved rapidly, the second NIR spectral region (NIR-II, 1000–1700 nm) window fluorescence bioimaging was verified to exhibit better spatial resolution, higher signal-to-background ratio (SBR), and deeper penetration depth compared to the conventional first NIR spectral region (NIR-I, 700–900 nm) window in more and more studies [14–18]. To date, several kinds of NIR-II fluorescence probes, including quantum dots (QDs) [17,19,20], carbon nanotubes [21–23], aggregation-induced emission (AIE) dots [24–27], and rare-earth nanoparticles [28–30], have been employed for outstanding NIR-II fluorescence whole-body and microscopic imaging. However, most of them confronted the same challenge in the process of clinical translation for their uncertain pharmacokinetic/toxicokinetic and drug metabolism [4,31,32]. Therefore, there is an urgent demand for NIR dyes which balances the advantages of NIR-II imaging and clinical applicability. So far, it was only a clinically approved NIR dye indocyanine green (ICG) that has shown potential in clinical NIR-II

* Corresponding authors.
E-mail addresses: qianjun@zju.edu.cn (J. Qian), 3193119@zju.edu.cn (G. Li).

https://doi.org/10.1016/j.eng.2021.07.032

fluorescence imaging based on its NIR-II emission tail [15,16,33] but limited to be applied in the imaging of the hepatobiliary system and lymphatic system.

Methylene blue (MB), a renal excretable NIR-I dye approved by the US Food and Drug Administration (FDA), has been extensively adopted for NIR-I fluorescence imaging-guided surgeries such as the identification of ureter, localization of insulinoma and normal pancreas, and intraoperative detection of breast cancer [34–37]. Intriguingly, the excellent molar extinction coefficient (71 200 $L{\cdot}mol^{-1}{\cdot}cm^{-1}$ at peak absorbance (665 nm)) and relatively high quantum yield (QY, 3.8%) [34] made MB a candidate for clinical NIR-II fluorescence imaging. Unfortunately, to the best of our knowledge, the application of MB in NIR-II fluorescence bioimaging has not been reported yet.

Herein, we successfully detected the NIR-II emission tail of MB and compared tissue penetrating capability in the NIR-I window and NIR-II window by imaging capillary tubes filled with MB aqueous solution submerged in Intralipid® 1% solution *in vitro*. Subsequently, *in vivo* comparison of UCG and excretory urography in the NIR-I and NIR-II windows were performed in the mouse models. Moreover, MB with a bright NIR-II emission tail also made noninvasive evaluation of renal function in the mouse model feasible. Our study aims to evaluate the validity and feasibility of applying MB to the structural and functional NIR-II bioimaging in the urinary system and provide a brand new potential translation of NIR-II imaging into clinical and preclinical applications.

2. Material and methods

2.1. Materials

Clinical grade MB was purchased from Jumpcan Pharmaceutical Factory (China). Phosphate buffer saline (PBS) was obtained from Sinopharm Chemical Reagent Co., Ltd. (China). Intralipid® 20% was purchased from Baxter Healthcare Corporation (USA). Deionized (DI) water with a resistivity of 18.2 $M\Omega{\cdot}cm^{-1}$ was used in all experiments.

2.2. Absorption and fluorescence emission characterization

Measurement of absorption spectra of MB in aqueous solution was obtained from 550 to 900 nm using a Shimadzu UV-2550 ultraviolet–visible–NIR scanning spectrophotometer (Shimadzu, Japan). The fluorescence emission spectra of MB dilutions in water and urine in the NIR-II window were measured by a laboratory-built system based on a PG2000 spectrometer (Ideaoptics Instruments, China) and a 2000C spectrometer (Everuping Optics Corporation, China).

2.3. Quantum yield measurement

The QY of MB aqueous solution was measured using an NIR-II dye IR-26 in dichlorethane (DCE) as a reference (QY ≈ 0.5%) [38]. A series of DCE solutions of IR-26 and MB aqueous solution with different optical density (OD) values were measured under 623 nm excitation, and NIR-II fluorescence intensities were integrated beyond 1000 nm. Two slopes of the straight lines describing the dependence of integrated NIR-II fluorescence intensity upon OD (one from the reference of IR-26 in DCE and the other from the MB aqueous solution) were obtained. The QY of the sample (Q_2) was calculated by the equation as follows:

$$Q_2 = Q_1 \cdot \frac{F_{slope2}}{F_{slope1}} \cdot \frac{n_2^2}{n_1^2}$$

where Q_1 is the QY of IR-26 in DCE (0.5%), F_{slope1} is the slope value for IR-26 in DCE, F_{slope2} is the slope value for MB aqueous solution, n_1 is the refractive index of DCE, and n_2 is the refractive index of water.

2.4. The photostability assay

The photostability assay of MB aqueous solution (0.005 $mg{\cdot}mL^{-1}$) was conducted under continuous illumination from 623 nm light-emitting diode (LED) with a power density of 80 $mW{\cdot}cm^{-2}$ for 60 min. The average fluorescence intensity was calculated from the region of the cuvette.

2.5. Intralipid® phantom imaging

In vitro testing in an Intralipid® phantom was performed as described previously. Intralipid® 1% solution was prepared by diluting Intralipid® 20% into DI water. A capillary glass tube (inner diameter = 0.3 mm) filled with MB solution (0.005 $mg{\cdot}mL^{-1}$) was immersed in the prepared Intralipid® 1% solution, the depth of which ranged from 1 to 6 mm below the top surface. NIR-I and NIR-II imaging at different depths were performed (excitation wavelength: 623 nm; power density: 30 $mW{\cdot}cm^{-2}$; exposure time: 10 ms for NIR-I window versus 50 ms for NIR-II window).

2.6. Animal experiments

The present study was approved by the Animal Research Ethics Committee of Zhejiang University (IACUC: ZJU20160141) and all the animal experiments in this work were conducted strictly in compliance with the requirements and guidelines of the Institutional Ethical Committee of Animal Experimentation of Zhejiang University. Institute of Cancer Research (ICR) mice (6–8 weeks old, female) and BLAB/c Nude mice (6–8 weeks old, female) were provided from the Shanghai SLAC Laboratory Animal Corporation (China) and kept in the Laboratory Animal Center of Zhejiang University (China). The animal housing area was maintained at 24 °C with a 12 h light/dark cycle, with free water and food available. Before each operation and imaging experiment, mice were anesthetized via intraperitoneal injection of 2% pentobarbital (40–50 $mg{\cdot}kg^{-1}$ bodyweight) and kept in maintaining anesthesia. Mice were intravenously injected with MB aqueous solution (0.01 $mg{\cdot}g^{-1}$ bodyweight, intravenously) before excretory urography and were administrated irrigation of bladder using MB aqueous solution (0.005 $mg{\cdot}mL^{-1}$, 100 μL) before UCG.

2.7. NIR-I fluorescence imaging

Images in the NIR-I window were captured using GA1280 camera (1280 × 1024 pixels; Tekwin System, China) equipped with a prime lens (focal length 50 mm, antireflection coating at 800–2000 nm; Edmund Optics, USA), which was fitted with an 800 nm long-pass filter and a 900 nm short-pass filter to extract NIR-I fluorescence signal. A 623 nm LED was used to provide uniform illumination on the field of interest (Fig. S1(a) in Appendix A).

2.8. NIR-II fluorescence imaging

A two-dimensional (2D) electronic-cooling indium gallium arsenide (InGaAs) camera (640 × 512 pixels; Tekwin System) equipped with a prime lens (focal length 50 mm, antireflection coating at 800–2000 nm, Edmund Optics), cooled to −40 °C was used to acquire images in the NIR-II window (Fig. S1(b) in Appendix A). A 623 nm LED (SOLIS-623C; Thorlabs, USA) was used to provide uniform illumination on the imaging field. The facular power density was measured before each imaging experiment. During imaging, an 800 nm short-pass filter was used to filter 623 nm excitation. A 1000 nm long-pass filter (Thorlabs) was placed in

front of the camera lens restricting wavelength below as well as allowing wavelength above 1000 nm to pass through the camera lens.

2.9. In vivo *kidney and bladder structural imaging*

MB assisted UCG was conducted after the irrigation of the bladder using 200 μL MB aqueous solution (0.005 mg·mL^{-1}) and MB assisted excretory urography was conducted after intravenously injection of MB (0.01 mg·g^{-1} bodyweight) in living mice. The signals of kidneys (dorsal side) and bladders (ventral side) were acquired in both the NIR-I and NIR-II windows (623 nm LED, 80 mW·cm^{-2}).

2.10. In vivo *ureter imaging*

Mice were fixed on a platform in the supine position. Laparotomy was performed and the ureters were fully exposed. MB (0.01 mg·g^{-1} bodyweight) was intravenously injected into each mouse, and then a piece of abdominal tissue was placed on the ureter. NIR-I and NIR-II imaging were further performed to visualize the ureter through the covered tissue. For the acute ureter ligation model, the right ureter was ligated by surgical sutures. Likewise, MB at a concentration of 1 mg·mL^{-1} was intravenously injected through the tail vein instantly after ligation, and the facular power density was adjusted to 30 mW·cm^{-2}. The mice were observed using an NIR-I or NIR-II camera to localize the ureter and detect the ligation point covered by an abdominal tissue.

2.11. In vivo *renal functional imaging*

The unilateral ureteral obstruction (UUO) model was established to investigate the renal perfusion by using MB assisted NIR-II fluorescence imaging. Briefly, the UUO model was first established by complete ligation of the left ureter of the mouse while the right ureter was kept intact, and unilateral hydronephrosis and renal perfusion disorder gradually progressed over time. For the sham-operated group, the ureters were not ligated. Subsequently, NIR-II fluorescence imaging was conducted in the UUO-3d group (UUO for 3 days), the UUO-6d group (UUO for 6 days), and the sham-operated group after MB intravenously injection (0.01 mg·g^{-1} bodyweight). The profile for the signals in kidneys at different time points was recorded as a function of imaging time. On the other hand, the unilateral renal failure (URF) models were established to assess the renal filtration ability of MB assisted NIR-II fluorescence imaging. Briefly, the right kidneys (RKs) were excised both in the URF model and the sham-operated group, and the left kidneys (LKs) were injured by an electric coagulation knife to varying degrees in the URF model group but remained intact in the sham-operated group. NIR-II fluorescence imaging was conducted as mentioned above.

2.12. Serum creatinine and blood urea nitrogen assay

Blood was collected from the angular vein of the mice. The collected blood samples were centrifuged for 15 min at 4500 r·min^{-1}. Serum creatinine (Cre) and blood urea nitrogen (BUN) were determined using commercial kits according to the manufacturer's protocols.

2.13. Histopathologic study

The kidney tissues of the UUO groups and the sham-operated group were dissected and fixed with 4% paraformaldehyde, dehydrated in an ethanol solution, embedded in paraffin and cut into sections with a thickness of 15 μm for hematoxylin and eosin (H&E) staining. The sections were washed with xylene and ethanol, and then immersed in hematoxylin working solution for 4 min and eosin working solution for 2 min, followed by washing with distilled water. The stained sections were examined using a microscope (Primovert; Zeiss, Germany).

2.14. Data analysis

Quantitative analysis of each fluorescent image was performed based on the measurement of mean signal intensity in the manually selected regions of interest, using ImageJ software (Version 1.6.0; National Institutes of Health, USA). Graphs were generated using OriginPro software (Version 9.0; OriginLab Company, USA). The data are presented as mean ± standard deviation (SD). Statistical analysis was performed using Student's *t*-test. * denotes a statistical significance ($^*p < 0.05$, $^{**}p < 0.01$, and $^{***}p < 0.001$) between the experiment data of the two groups.

3. Results and discussion

3.1. MB optical characterization

MB, a small molecule NIR-I dye (the chemical structure was shown in Fig. 1(a)), had an absorbance peak at ~665 nm. The emission spectrum of MB aqueous solution was recorded on a silicon (Si) and an InGaAs detector-based spectrometer, indicating that its fluorescence emission extended into NIR-II window (Figs. 1(b) and (c)). Beyond a wavelength of 1000 nm, the QY of MB in water was calculated as 0.2% (Fig. S2 in Appendix A), which is based on the NIR-II fluorescence QY (~0.5%) of IR-26 in DCE as the reference. Importantly, MB showed higher NIR-II fluorescence intensity under 623 nm LED excitation (0.1 mg·mL^{-1}, 30 mW·cm^{-2}) than another reported renal-clearable NIR-II dye (CH-1055-PEG [39]) under 793 nm laser excitation (0.1 mg·mL^{-1}, 30 mW·cm^{-2}), as illustrated in Fig. S3 in Appendix A. Besides, MB in water also showed negligible fluorescence decay under continuous 623 nm LED irradiation (80 mW·cm^{-2}) for 60 min, exhibiting an excellent photostability (Fig. S4 in Appendix A). To compare the fluorescence penetrating ability of MB in the NIR-I and NIR-II windows, a tissue phantom study using Intralipid® mimicking the optical characteristics of biological tissues was performed. The fluorescence signals decreased both in NIR-I and NIR-II window with increasing thickness of Intralipid® 1% solution. The NIR-I fluorescence signal of MB was close to the background noise at a 3 mm thickness of Intralipid® 1% solution while the NIR-II fluorescence signal for MB was still visible even at a thickness of 5 mm. Full-width-half-maximum (FWHM) analysis depicting the feature width of NIR-I and NIR-II capillary images at varying depths in Intralipid® phantom assay was also plotted (Fig. 1(d)): The fluorescence FWHM measurement of the capillary tube without Intralipid® 1% solution were (386.5 ± 5.4) and (389.4 ± 1.7) μm in the NIR-I and NIR-II window, respectively. Whereas the FWHM was (3294.9 ± 453.2) and (1243.1 ± 14.4) μm in the NIR-I and NIR-II windows, respectively, when the depth increased to 6 mm (Fig. 1(e)). Besides, the SBRs for MB in NIR-II window were 1.7-, 4.3-, 2.7-, 2.1-, and 1.8-fold higher than those for MB in the NIR-I window at a Intralipid® 1% solution thickness of 1, 2, 3, 4, and 5 mm, respectively (Fig. 1(f)). These results indicated that the fluorescence of MB in the NIR-II window had deeper tissue penetration and higher sensitivity than those in the NIR-I window on account of the reduced light scattering in the NIR-II window.

3.2. MB assisted UCG in the NIR-I and NIR-II windows

Vesicoureteral reflux (VUR) is a common disease in children's urology. Due to the reflux of urine from the bladder to the ureter

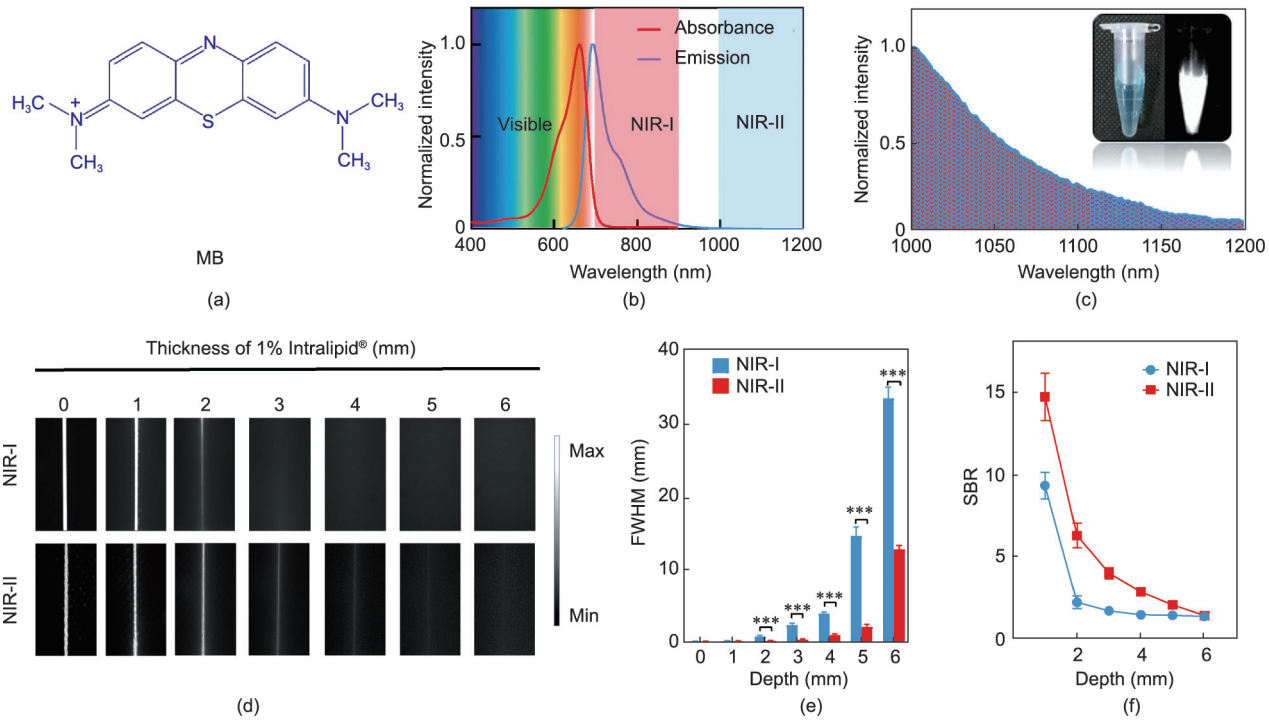

Fig. 1. Characterization of MB. (a) Chemical structure of MB. (b) Normalized absorption and emission spectra of MB in water. (c) Normalized fluorescence emission profile of MB between 1000 and 1200 nm wavelength region. (d) NIR-I and NIR-II fluorescence images of glass capillary filled with MB (0.005 mg·mL^{-1}) at depths of 0, 1, 2, 3, 4, 5, and 6 mm in Intralipid® 1% solution (excitation wavelength: 623 nm; power density: 30 mW·cm^{-2}; exposure time: 10 ms for NIR-I window versus 50 ms for NIR-II window). (e) FWHM and (f) SBR were calculated for capillary glass tubes filled with MB solution. Data are the mean ± SD, n = 3 independent measurements.

and renal pelvis during urination, it can progress to repeated urinary tract infections, which eventually leads to scarring, atrophy, and renal function of the kidneys [40]. UCG is the gold standard for the diagnosis of VUR. As VUR is an intermittent disease, it often requires multiple reflux assessment tests. However, currently available UCG techniques are all exposed to radiation, which results in the invisible increases in the carcinogenic risk for patients, especially for children [41]. Therefore, we tried to use MB assisted fluorescence imaging technology to achieve the UCG. We initially investigated the stability of MB in urine, and the fluorescence of MB exhibited minimal changes when diluted with mouse urine compared to MB aqueous solution at the same concentration (Figs. 2(a) and (b)). Subsequently, we conducted MB assisted UCG in the NIR-I and NIR-II windows after irrigation of the bladder with MB aqueous solution. Although MB has stronger fluorescence signal in the NIR-I window than that in the NIR-II window under the same imaging conditions, the SBR in the NIR-I window (1.23) was significantly lower than in the NIR-II window (2.26), which was consistent with the results of previous *in vitro* experiments, and MB assisted UCG in the NIR-II window can clearly and accurately reflected the size and boundary of the bladder (Figs. 2(c) and (d)).

According to the above results, we suggested that MB assisted fluorescence imaging was a promising technique for clinical UCG. Moreover, MB assisted UCG in the NIR-II window has more imaging advantages, compared to that conducted in the NIR-I window.

3.3. *Excretion and* in vivo *stability of MB*

Before the MB assisted excretory urography and functional imaging experiments, we first investigated its excretion. As is shown in Fig. S5 in Appendix A, NIR-II fluorescence signals mainly located in the bladder and the gallbladder of mice intravenously injected with MB aqueous solutions (30 min postinjection), which demonstrated that MB could be excreted by kidney and liver as reported in previous studies [42,43]. Subsequently, the whole-body NIR-II fluorescence imaging (dorsal and ventral side) was conducted at different post-treatment time points after intravenous injection of MB (Figs. 3(a) and (b)). The signals in the kidneys reached the peak at 3 min post-injection of MB and then decreased with time while fluorescence signals in the bladder increased with time (Fig. 3(c)). Taken together, MB showed a potential for real-time NIR-II fluorescence visualization of the urinary system including structural and functional imaging.

3.4. *Excretory urography* in vivo *using MB in the NIR-I and NIR-II window*

The NIR-II emission and renal excretability enable MB a straightforward application to NIR-II fluorescence excretory urography. We first conducted non-invasive excretory kidney imaging using NIR-I and NIR-II imaging systems in the same mouse model. It was obvious that imaging using NIR-II detection had advantages over conventional NIR-I detection, with imaging in the NIR-II window achieving higher-contrast macroscopic imaging of the kidney in mice through intact skin compared with that in the NIR-I window (Figs. 4(a)–(c)).

Ureter injury is a rare but serious complication of urinary surgery; however, the diagnosis of such injury is often delayed [44–46]. Thus, early identification of ureteral is essential to avoid morbidity and preserve renal function. MB was reported to be successfully utilized in the intraoperative ureter visualization in the NIR-I window [35,37]. We, therefore, detected the feasibility of NIR-II fluorescence imaging application in the ureter identification compared with the NIR-I window. Invasive NIR-I and NIR-II fluorescence imaging were applied to the real-time identification of ureter covered by a mouse abdominal tissue (thickness:

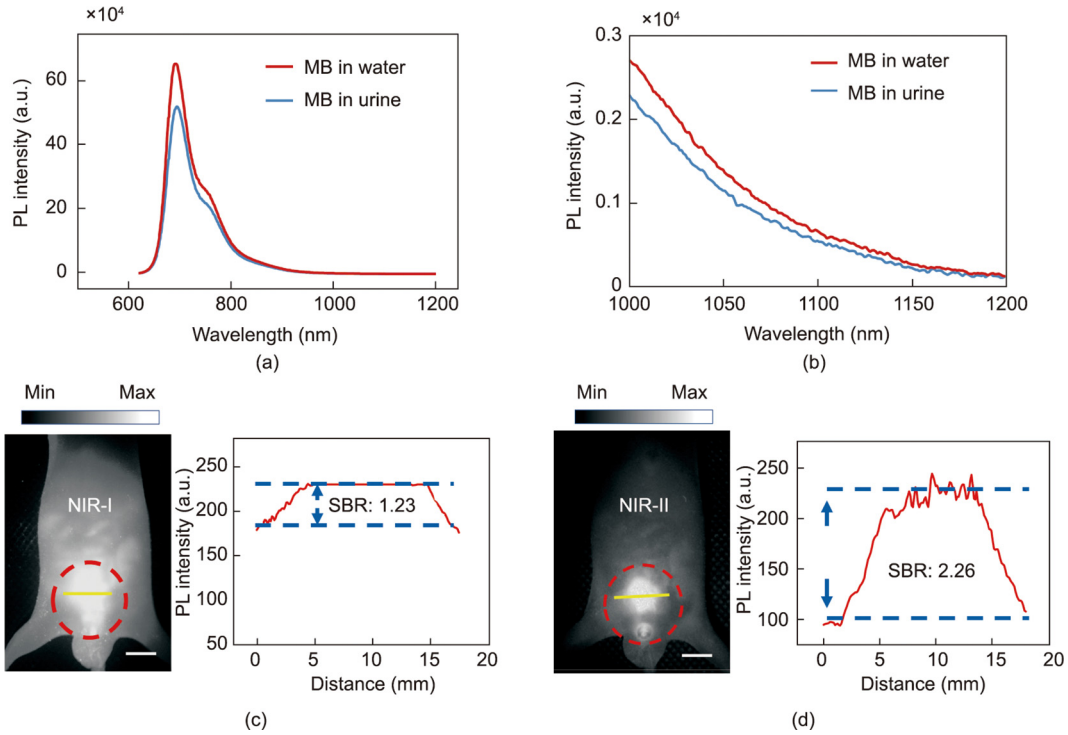

Fig. 2. MB assisted UCG in the NIR-I and NIR-II window. (a, b) Emission spectra of MB aqueous solution and MB in urine at the same concentration (0.005 mg·mL^{-1}). PL: Photoluminescence. Representative (c) NIR-I and (d) NIR-II fluorescence images of the bladders (excitation wavelength: 623 nm; power density: 80 mW·cm^{-2}; exposure time: 5 ms for NIR-I window versus 25 ms for NIR-II window. MB 0.005 mg·mL^{-1} (50 μL), bladder) and SBR analyses in the two windows, respectively. a.u.: arbitrary unit.

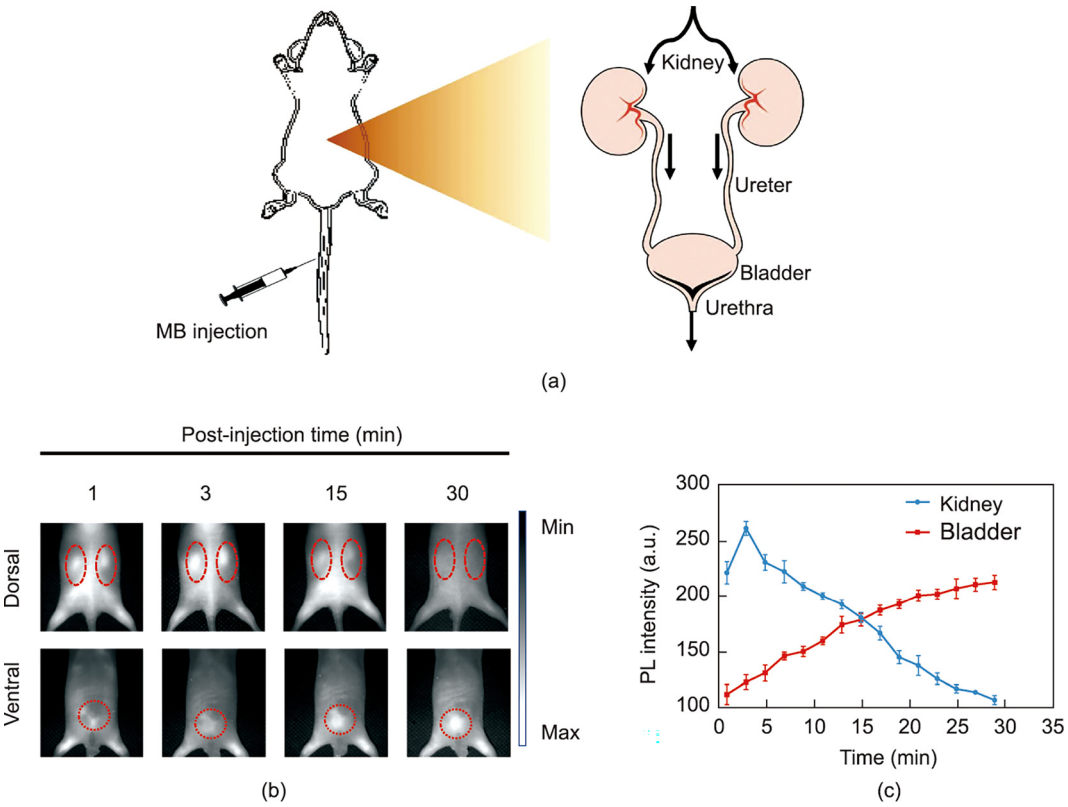

Fig. 3. Renal clearance and *in vivo* stability studies of MB. (a) Schematic illustration of the renal excretion of MB through the urinary system. (b) Representative NIR-II fluorescence images at t = 1, 3, 15, 30 min after injection of MB in mice. The red circles indicate the kidneys and bladder on the dorsal and ventral sides, respectively. NIR-II fluorescence images were acquired beyond 1000 nm upon excitation of 623 nm, LED power of ~80 mW·cm^{-2}. (c) NIR-II time-fluorescence intensity curves (TFICs) of the kidney and bladder after MB injection. Data are the mean ± SD, n = 3 independent measurements.

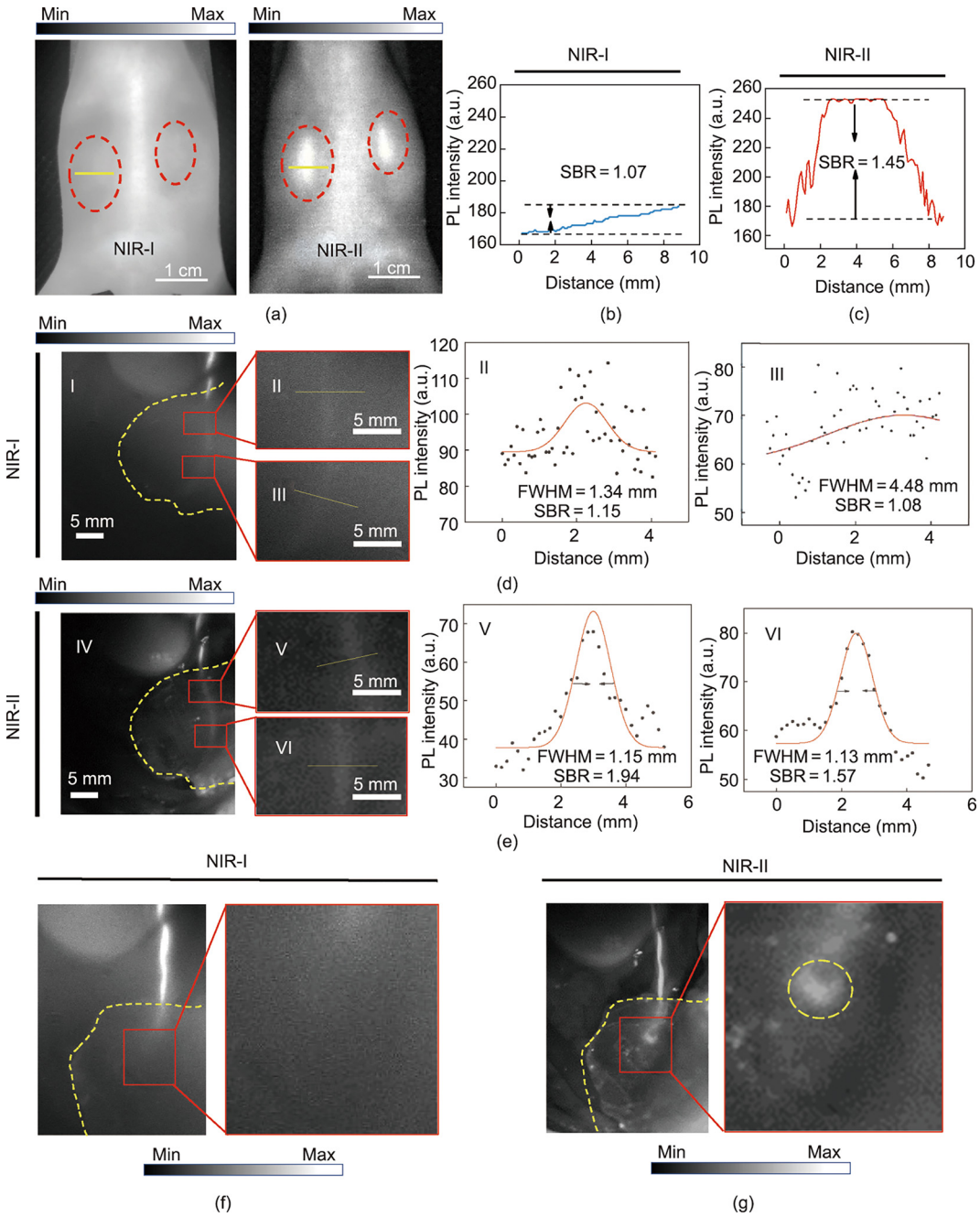

Fig. 4. Excretory urography based on MB in NIR-I and NIR-II windows. (a) Representative NIR-I and NIR-II fluorescence images of the kidneys (0.01 mg·g^{-1} bodyweight, intravenously). (b, c) SBR analyses in (b) NIR-I and (c) NIR-II window, respectively. (d, e) Representative images of ureter covered by mouse abdominal tissue after intravenous injection of MB in (d) NIR-I and (e) NIR-II window, FWHM and SBR of the ureter imaging in NIR-I and NIR-II window were calculated based on a two-term Gaussian fit to the intensity profiles. (f, g) Ureter imaging in the UUO model in (f) NIR-I window and (g) NIR-II window, yellow circle indicates the position of the obstruction point.

~1.5 mm) in the region of interest. Though the ureter could be visualized in the NIR-I window, the SBRs were rather low (Fig. 4(d)). When switching to the NIR-II window with a 1000 nm long-pass filter, the background noise significantly reduced and spatial resolution improved (Fig. 4(e)). Whereafter, acute ureter obstruction was established on a mouse model to identify ureter lesion under NIR-I and NIR-II detectors. As shown in Figs. 4(f) and (g), the ligation point of the ureter was identified with good contrast in the NIR-II window while the specific ligation point could be hardly recognized under the NIR-I detection after upregulating the penetrating depth. These results indicated that MB assisted NIR-II fluorescence imaging was a superior choice in image-guided surgery concerning ureter identification compared to the conventional NIR-I fluorescence imaging, especially for the patient whose ureter was covered by some tissues. As full clinical implementation of MB has been partially limited when the ureter was covered by adhesion tissue, the higher contrast of MB assisted NIR-II fluorescence imaging over NIR-I imaging could benefit these applications. Importantly, the implementation of this contrast improvement would be straightforward, requiring only a switch from cameras with NIR-I sensitivity to those with NIR-II sensitivity while maintaining the familiar surgical setup and MB use.

3.5. In vivo *MB assisted NIR-II fluorescence imaging of renal function*

Renal functional test or imaging usually reflects two aspects, those are, renal perfusion and renal filtration function. As the renal clearance is the main extracted way of MB and its fluorescence signal changes in kidneys could be detected non-invasively in the NIR-II window, MB seemed a good candidate for real-time imaging of renal function. Hence, the UUO model was first established for 3 and 6 d (Fig. 5(a)) by complete ligation of the left ureter of the mouse while the right ureter was kept intact (Fig. 5(b)). As a result, unilateral hydronephrosis and renal perfusion disorder gradually progressed over time. For the sham-operated group, the ureters were not ligated. Subsequently, NIR-II fluorescence imaging was conducted in the UUO-3d group, the UUO-6d group, and the sham-operated group, and the profile for the signals in kidneys at different time points was recorded (Fig. 5(c)). With MB as the NIR-II contrast agent,

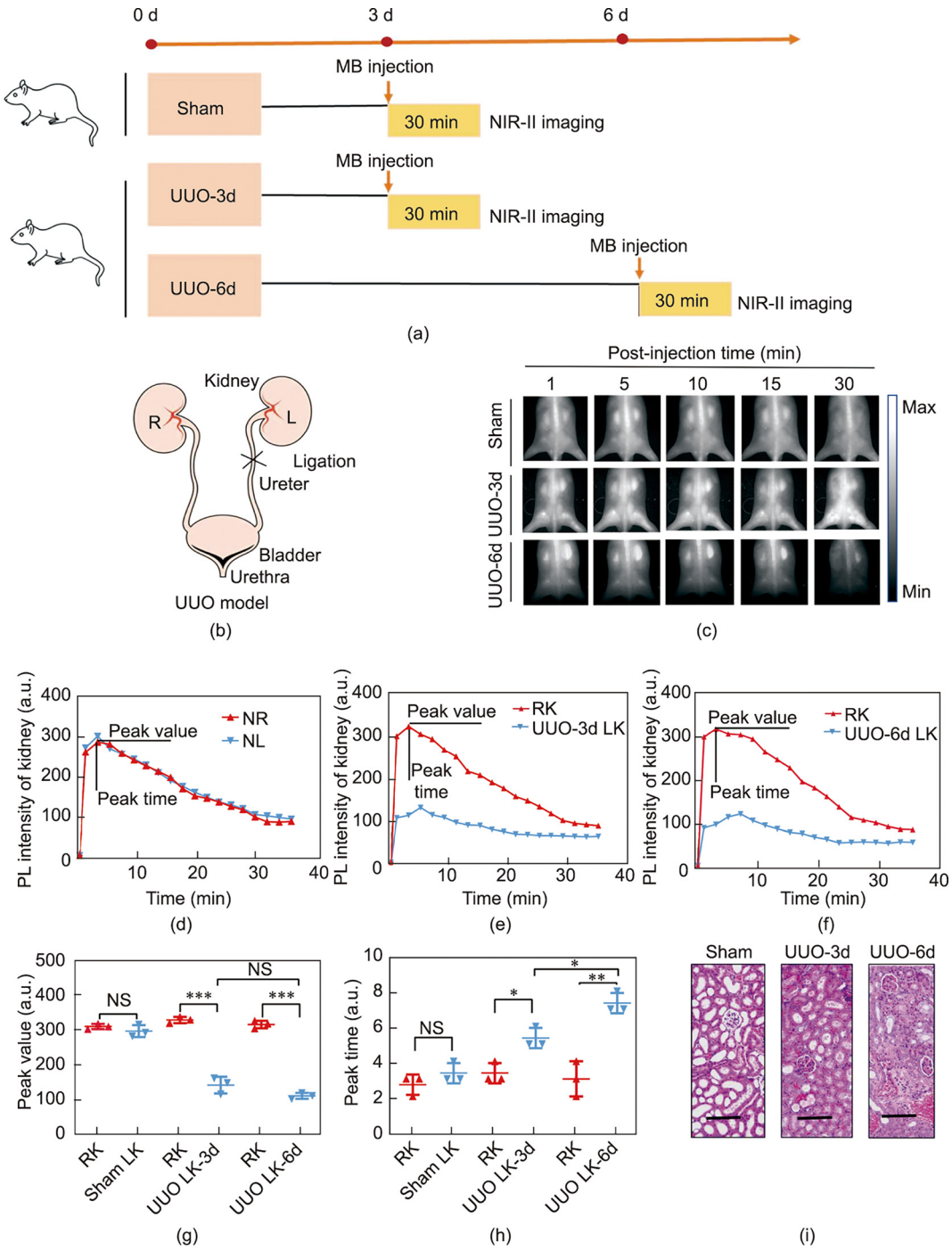

Fig. 5. Real-time detection of kidney blood perfusion via NIR-II fluorescence imaging of MB in living mice. (a) Schematic illustration of mice of the sham-operated group and UUO group, and NIR-II fluorescence imaging at different post-operation time points. (b) Schematic illustration of UUO model establishment by complete ligation of the left ureter while the right ureter was kept intact. (c) Representative whole-body (dorsal side) noninvasive fluorescence images of mice after intravenous injection of MB solution (0.01 mg·g^{-1} bodyweight, intravenously) at different post-injection time points (wavelength: 623 nm; power density: 80 mW·cm^{-2}; exposure time: 60 ms). (d–f) TFICs of kidneys in (d) the sham-operated group, (e) the UUO-3d group, and (f) the UUO-6d group. (g, h) Statistical analysis of the two parameters extracted from the kidney TFICs of UUO mice and the sham-operated group. The parameters include the (g) peak value and (h) the peak time. Data are the mean ± SD. n = 3 independent measurements. $^{*}p < 0.05$, $^{**}p < 0.01$, $^{***}p < 0.001$. (i) Kidney pathologic analysis of the sham-operated group, UUO-3d group, and UUO-6d group (H&E stain, scale bar = 100 μm). NS: not significance.

we easily differentiated the UUO kidneys from the normal kidneys by noninvasive NIR-II imaging and analysis of the time-fluorescence intensity curves (TFICs) of the kidneys. As shown in Figs. 5(d) and (f), the signal changes of the LK and RK showed no significant differences in the sham-operated group (Fig. 5(d)) while the obstructed LKs showed dramatically decreased signal peak value compared to the normal RKs in the UUO groups (Fig. 5(g)). Correspondingly, the peak time of the obstructed LK TFIC was delayed in the UUO groups compared to the normal RK in UUO groups and the kidneys in the sham-operated group (Fig. 5(h)). Moreover, the obstructed LK signals in the UUO-6d group showed a prolonged peak time compared to those in the UUO-3d group, which was consistent with the pathological analysis of kidney tissues (Fig. 5(i)): The renal tubules exhibited mild to moderate atrophy and dilatation in kidneys of the UUO-3d group which suggested mild renal perfusion disorder, whereas, renal tubular damage and cortical atrophy were much more pronounced in kidneys of the UUO-6d group. These data indicated that MB assisted NIR-II fluorescence imaging of renal function could not only differentiate between normal kidneys and kidneys with perfusion disorder but also reflected the severe stage of the perfusion disorder.

Renal filtration function is also indispensable for the renal function analysis, and BUN and Cre are frequently used to evaluate the renal filtration function, but they both are not good indicators of a single kidney because of the presence of a well-functioning contralateral kidney. Given this compensatory mechanism, the solitary kidney models were established by right nephrectomy, which was used to investigate the feasibility of MB assisted NIR-II real-time imaging in the assessment of renal filtration function. Further, the LKs were treated with varying degrees of electric coagulation injury in the URF group but were kept intact in the sham-operated group (Fig. 6(a)). Similarly, MB assisted NIR-II real-time imaging was carried out after MB intravenously injection with TFICs utilized to analyze the renal filtration function (defined as the clearance percentage at 30 min = peak value intensity at 30 min/peak value × 100%) (Figs. 6(b) and (c)). As is shown in Fig. 6(d), MB

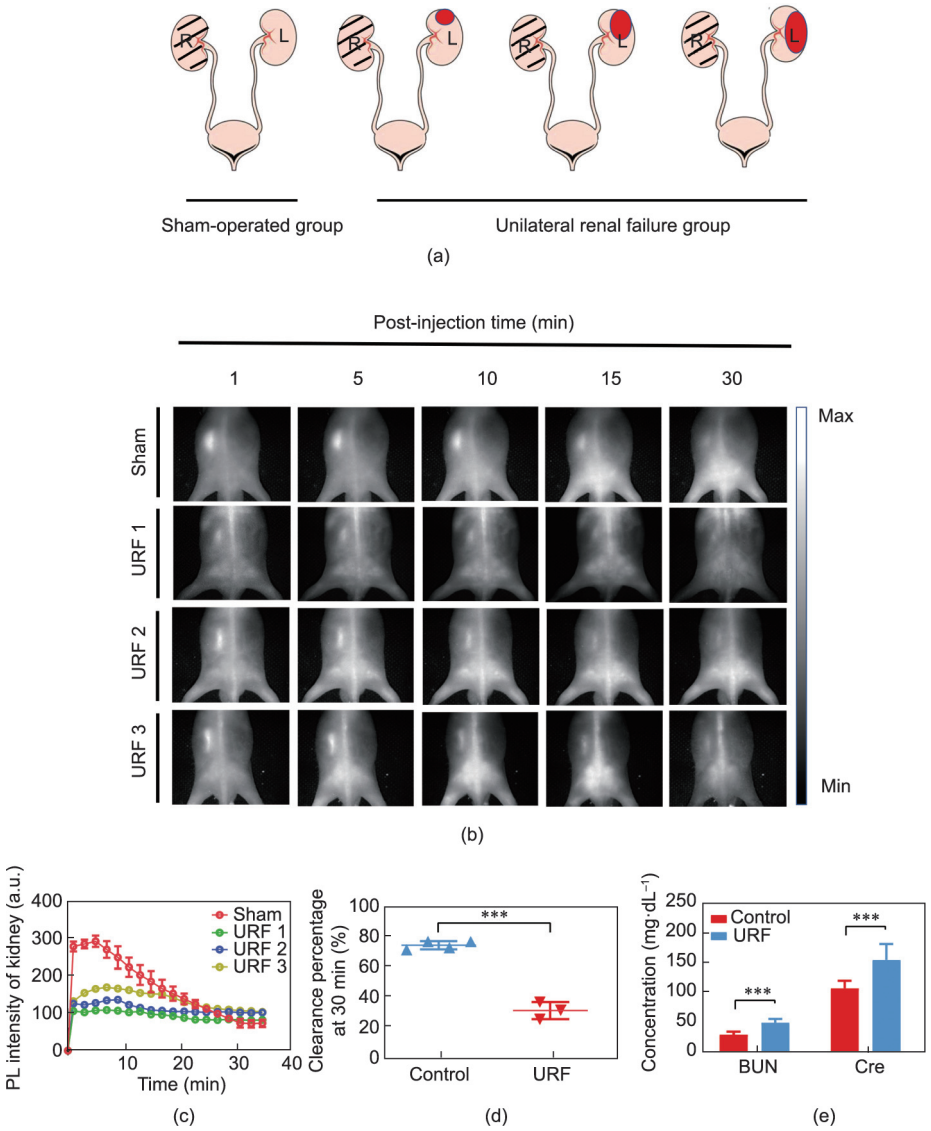

Fig. 6. Real-time detection of renal filtration function via NIR-II fluorescence imaging of MB in living mice. (a) Schematic illustration of URF model establishment; red areas indicate lesion sites by electrical coagulation. (b) Representative NIR-II fluorescence images of the control group and URF group after intravenous injection of MB (0.01 mg·g^{-1} bodyweight, intravenously) at different post-injection time points (excitation wavelength: 623 nm; power density: 80 mW·cm^{-2}; exposure time: 60 ms). (c) TFICs of kidneys in the control group and URF group. (d) Statistical analysis of the clearance percentage at 30 min extracted from the kidney TFICs of the control group and the URF group, ***p < 0.001. (e) *In vitro* detection of renal function with other assays (Cre and BUN) in the control group and the URF group, ***p < 0.001.

clearance percentage at 30 min was reduced significantly in the URF group compared to the sham-operated group. To compare the renal function detection ability of MB with the clinical methods, Cre and BUN in the blood of living mice were measured using the commercial assays in the two groups. Statistically significant increases both in Cre and BUN were observed in the URF group. These data were consistent with the above imaging results, suggesting that MB is feasible for noninvasively detecting renal filtration function by NIR-II fluorescence imaging.

Although several NIR-II dyes such as CH-1055-PEG, CDIR2, rare-earth nanoparticles, and gold nanoparticles were reported to show potential in the NIR-II imaging of renal function [39,47–51], considerable work is required to use them in *in vivo* application because of uncertain toxicity and pharmacokinetics. Moreover, the power densities of the excitation laser were fairly high in real-time imaging even for animal models (300 $mW{\cdot}cm^{-2}$ for both CDIR2 and CH-1055-PEG) [39,50]. Nevertheless, MB could achieve clear real-time imaging at a relatively low power density of 623 nm LED excitation (80 $mW{\cdot}cm^{-2}$). As the absorbance of MB at 665 nm was 1.85-fold higher than that at 623 nm, clear MB real-time imaging may be achieved at an even lower power density at 665 nm excitation.

4. Conclusions

In summary, we detected the NIR-II emission of MB and investigated its application in NIR-II fluorescence invasive/noninvasive urography and noninvasive NIR-II imaging of renal function in mouse models for the first time. MB showed higher SBR and better spatial resolution in the NIR-II window than in the NIR-I window, which suggested a more appropriate detection window when using MB fluorescence imaging clinically: Switching the traditional silicon-based detection cameras to emerging InGaAs cameras could potentially improve the fluorescence imaging technique both preoperatively and intraoperatively. As MB is excreted mainly through the kidney, the renal function analysis of MB assisted NIR-II fluorescence imaging is consistent with the pathology result and clinical diagnostic parameters including Cre and BUN. Thus, MB assisted NIR-II fluorescence imaging not only holds great promise for invasive and noninvasive structural imaging of the urinary system clinically but also permits investigation of renal function preclinically.

Acknowledgments

This work was supported by the National Natural Science Foundation of China (81672520, 81870484, 61975172, and 82001874, used for procurement of materials and labor cost), Science and Technology Planning Project of Zhejiang (2019C03089, used for procurement of materials), and Zhejiang Provincial Natural Science Foundation of China (LR17F050001, used for procurement of materials).

Compliance with ethics guidelines

Dingwei Xue, Di Wu, Zeyi Lu, Jochen Neuhaus, Abudureheman Zebibula, Zhe Feng, Sheng Cheng, Jing Zhou, Jun Qian, and Gonghui Li declare that they have no conflict of interest or financial conflicts to disclose.

Appendix A. Supplementary data

Supplementary data to this article can be found online at https://doi.org/10.1016/j.eng.2021.07.032.

References

[1] Essman SC. Contrast cystography. Clin Tech Small Anim Pract 2005;20(1):46–51.
[2] McDonald RJ, McDonald JS, Carter RE, Hartman RP, Katzberg RW, Kallmes DF, et al. Intravenous contrast material exposure is not an independent risk factor for dialysis or mortality. Radiology 2014;273(3):714–25.
[3] Bjurlin MA, Turkbey B, Rosenkrantz AB, Gaur S, Choyke PL, Taneja SS. Imaging the high-risk prostate cancer patient: current and future approaches to staging. Urology 2018;116:3–12.
[4] Moosavi B, Shabana WM, El-Khodary M, van der Pol CB, Flood TA, McInnes MDF, et al. Intracellular lipid in clear cell renal cell carcinoma tumor thrombus and metastases detected by chemical shift (in and opposed phase) MRI: radiologic-pathologic correlation. Acta Radiol 2016;57(2):241–8.
[5] Morris MJ, Autio KA, Basch EM, Danila DC, Larson S, Scher HI. Monitoring the clinical outcomes in advanced prostate cancer: what imaging modalities and other markers are reliable? Semin Oncol 2013;40(3):375–92.
[6] Chawla LS, Eggers PW, Star RA, Kimmel PL. Acute kidney injury and chronic kidney disease as interconnected syndromes. N Engl J Med 2014;371(1):58–66.
[7] Taylor AT, Lipowska M, Cai H. $^{99m}Tc(CO)_3$(NTA) and ^{131}I-OIH: comparable plasma clearances in patients with chronic kidney disease. J Nucl Med 2013;54(4):578–84.
[8] Grenier N, Basseau F, Ries M, Tyndal B, Jones R, Moonen C. Functional MRI of the kidney. Abdom Imaging 2003;28(2):164–75.
[9] Taylor AT. Radionuclides in nephrourology, part 1: radiopharmaceuticals, quality control, and quantitative indices. J Nucl Med 2014;55(4):608–15.
[10] Cheng D, Peng J, Lv Y, Su D, Liu D, Chen M, et al. *De novo* design of chemical stability near-infrared molecular probes for high-fidelity hepatotoxicity evaluation *in vivo*. J Am Chem Soc 2019;141(15):6352–61.
[11] Feng Z, Yu X, Jiang M, Zhu L, Zhang Y, Yang W, et al. Excretable IR-820 for *in vivo* NIR-II fluorescence cerebrovascular imaging and photothermal therapy of subcutaneous tumor. Theranostics 2019;9(19):5706–19.
[12] Sun C, Li B, Zhao M, Wang S, Lei Z, Lu L, et al. J-aggregates of cyanine dye for NIR-II *in vivo* dynamic vascular imaging beyond 1500 nm. J Am Chem Soc 2019;141(49):19221–5.
[13] Hori Y, Otomura N, Nishida A, Nishiura M, Umeno M, Suetake I, et al. Synthetic-molecule/protein hybrid probe with fluorogenic switch for live-cell imaging of DNA methylation. J Am Chem Soc 2018;140(5):1686–90.
[14] Ding F, Zhan Y, Lu X, Sun Y. Recent advances in near-infrared II fluorophores for multifunctional biomedical imaging. Chem Sci 2018;9(19):4370–80.
[15] Zhu S, Hu Z, Tian R, Yung BC, Yang Q, Zhao S, et al. Repurposing cyanine NIR-I dyes accelerates clinical translation of near-infrared-II (NIR-II) bioimaging. Adv Mater 2018;30(34):e1802546.
[16] Carr JA, Franke D, Caram JR, Perkinson CF, Saif M, Askoxylakis V, et al. Shortwave infrared fluorescence imaging with the clinically approved near-infrared dye indocyanine green. Proc Natl Acad Sci USA 2018;115(17):4465–70.
[17] Zebibula A, Alifu N, Xia L, Sun C, Yu X, Xue D, et al. Ultrastable and biocompatible NIR-II quantum dots for functional bioimaging. Adv Funct Mater 2018;28(9):1703451.
[18] Del Rosal B, Villa I, Jaque D, Sanz-Rodríguez F. *In vivo* autofluorescence in the biological windows: the role of pigmentation. J Biophotonics 2016;9(10):1059–67.
[19] Zhang M, Yue J, Cui R, Ma Z, Wan H, Wang F, et al. Bright quantum dots emitting at ~1,600 nm in the NIR-IIb window for deep tissue fluorescence imaging. Proc Natl Acad Sci USA 2018;115(26):6590–5.
[20] Hong G, Robinson JT, Zhang Y, Diao S, Antaris AL, Wang Q, et al. *In vivo* fluorescence imaging with Ag_2S quantum dots in the second near-infrared region. Angew Chem Int Ed Engl 2012;51(39):9818–21.
[21] Diao S, Hong G, Robinson JT, Jiao L, Antaris AL, Wu JZ, et al. Chirality enriched (12,1) and (11,3) single-walled carbon nanotubes for biological imaging. J Am Chem Soc 2012;134(41):16971–4.
[22] Robinson JT, Hong G, Liang Y, Zhang B, Yaghi OK, Dai H. *In vivo* fluorescence imaging in the second near-infrared window with long circulating carbon nanotubes capable of ultrahigh tumor uptake. J Am Chem Soc 2012;134(25):10664–9.
[23] Hong G, Diao S, Chang J, Antaris AL, Chen C, Zhang B, et al. Through-skull fluorescence imaging of the brain in a new near-infrared window. Nat Photonics 2014;8(9):723–30.
[24] Li Y, Cai Z, Liu S, Zhang H, Wong STH, Lam JWY, et al. Design of AIEgens for near-infrared IIb imaging through structural modulation at molecular and morphological levels. Nat Commun 2020;11(1):1255.
[25] Zheng Z, Li D, Liu Z, Peng HQ, Sung HHY, Kwok RTK, et al. Aggregation-induced nonlinear optical effects of AIEgen nanocrystals for ultradeep *in vivo* bioimaging. Adv Mater 2019;31(44):e1904799.
[26] Alifu N, Zebibula A, Qi J, Zhang H, Sun C, Yu X, et al. Single-molecular near-infrared-II theranostic systems: ultrastable aggregation-induced emission nanoparticles for long-term tracing and efficient photothermal therapy. ACS Nano 2018;12(11):11282–93.
[27] Qi J, Sun C, Zebibula A, Zhang H, Kwok RTK, Zhao X, et al. Real-time and high-resolution bioimaging with bright aggregation-induced emission dots in short-wave infrared region. Adv Mater 2018;30(12):e1706856.
[28] Wang R, Li X, Zhou L, Zhang F. Epitaxial seeded growth of rare-earth nanocrystals with efficient 800 nm near-infrared to 1525 nm short-wavelength infrared downconversion photoluminescence for *in vivo* bioimaging. Angew Chem Int Ed Engl 2014;53(45):12086–90.

[29] Wang P, Fan Y, Lu L, Liu L, Fan L, Zhao M, et al. NIR-II nanoprobes *in-vivo* assembly to improve image-guided surgery for metastatic ovarian cancer. Nat Commun 2018;9(1):2898.
[30] Naczynski DJ, Tan MC, Zevon M, Wall B, Kohl J, Kulesa A, et al. Rare-earth-doped biological composites as *in vivo* shortwave infrared reporters. Nat Commun 2013;4(1):2199.
[31] Alshehri R, Ilyas AM, Hasan A, Arnaout A, Ahmed F, Memic A. Carbon nanotubes in biomedical applications: factors, mechanisms, and remedies of toxicity. J Med Chem 2016;59(18):8149–67.
[32] Wang Y, Hu R, Lin G, Roy I, Yong KT. Functionalized quantum dots for biosensing and bioimaging and concerns on toxicity. ACS Appl Mater Interfaces 2013;5(8):2786–99.
[33] Yu X, Feng Z, Cai Z, Jiang M, Xue D, Zhu L, et al. Deciphering of cerebrovasculatures via ICG-assisted NIR-II fluorescence microscopy. J Mater Chem B 2019;7(42):6623–9.
[34] Winer JH, Choi HS, Gibbs-Strauss SL, Ashitate Y, Colson YL, Frangioni JV. Intraoperative localization of insulinoma and normal pancreas using invisible near-infrared fluorescent light. Ann Surg Oncol 2010;17(4):1094–100.
[35] Verbeek FPR, van der Vorst JR, Schaafsma BE, Swijnenburg RJ, Gaarenstroom KN, Elzevier HW, et al. Intraoperative near infrared fluorescence guided identification of the ureters using low dose methylene blue: a first in human experience. J Urol 2013;190(2):574–9.
[36] Tummers QRJG, Verbeek FPR, Schaafsma BE, Boonstra MC, van der Vorst JR, Liefers GJ, et al. Real-time intraoperative detection of breast cancer using near-infrared fluorescence imaging and methylene blue. Eur J Surg Oncol 2014;40(7):850–8.
[37] Matsui A, Tanaka E, Choi HS, Kianzad V, Gioux S, Lomnes SJ, et al. Real-time, near-infrared, fluorescence-guided identification of the ureters using methylene blue. Surgery 2010;148(1):78–86.
[38] Semonin OE, Johnson JC, Luther JM, Midgett AG, Nozik AJ, Beard MC. Absolute photoluminescence quantum yields of IR-26 dye, PbS, and PbSe quantum dots. J Phys Chem Lett 2010;1(16):2445–50.
[39] Antaris AL, Chen H, Cheng K, Sun Y, Hong G, Qu C, et al. A small-molecule dye for NIR-II imaging. Nat Mater 2016;15(2):235–42.
[40] Penna FJ, Caldamone A, Koyle MA. Coming full circle with vesicoureteral reflux: from Hutch to bladder and bowel dysfunction. J Pediatr Urol 2017;13(2):189–91.
[41] Sodickson A, Baeyens PF, Andriole KP, Prevedello LM, Nawfel RD, Hanson R, et al. Recurrent CT, cumulative radiation exposure, and associated radiation-induced cancer risks from CT of adults. Radiology 2009;251(1):175–84.
[42] DiSanto AR, Wagner JG. Pharmacokinetics of highly ionized drugs I: methylene blue—whole blood, urine, and tissue assays. J Pharm Sci 1972;61(4):598–602.
[43] DiSanto AR, Wagner JG. Pharmacokinetics of highly ionized drugs II: methylene blue—absorption, metabolism, and excretion in man and dog after oral administration. J Pharm Sci 1972;61(7):1086–90.
[44] Datta S, Wheatstone S, Challacombe B. The acute management of iatrogenic urological injuries; strategies and mind-set for the urologist attending an unfamiliar operating theatre. BJU Int 2013;112(5):540–2.
[45] Brandes S, Coburn M, Armenakas N, McAninch J. Diagnosis and management of ureteric injury: an evidence-based analysis. BJU Int 2004;94(3):277–89.
[46] Delacroix Jr SE, Winters JC. Urinary tract injuries: recognition and management. Clin Colon Rectal Surg 2010;23(3):221.
[47] Yu M, Liu J, Ning X, Zheng J. High-contrast noninvasive imaging of kidney clearance kinetics enabled by renal clearable nanofluorophores. Angew Chem Int Ed Engl 2015;54(51):15434–8.
[48] Yu M, Zhou J, Du B, Ning X, Authement C, Gandee L, et al. Noninvasive staging of kidney dysfunction enabled by renal-clearable luminescent gold nanoparticles. Angew Chem Int Ed Engl 2016;55(8):2787–91.
[49] Huang J, Lyu Y, Li J, Cheng P, Jiang Y, Pu K. A renal-clearable duplex optical reporter for real-time imaging of contrast-induced acute kidney injury. Angew Chem Int Ed Engl 2019;58(49):17796–804.
[50] Huang J, Xie C, Zhang X, Jiang Y, Li J, Fan Q, et al. Renal-clearable molecular semiconductor for second near-infrared fluorescence imaging of kidney dysfunction. Angew Chem Int Ed Engl 2019;58(42):15120–7.
[51] Huang J, Weinfurter S, Daniele C, Perciaccante R, Federica R, Della Ciana L, et al. Zwitterionic near infrared fluorescent agents for noninvasive real-time transcutaneous assessment of kidney function. Chem Sci 2017;8(4):2652–60.